Journal of Materials Chemistry A

PAPER

View Article Online
View Journal | View Issue

Cite this: J. Mater. Chem. A, 2019, 7, 20302

Chelation-assisted formation of multi-yolk–shell Co_4N@carbon nanoboxes for self-discharge-suppressed high-performance Li–SeS_2 batteries†

Tao Chen,‡[a] Weihua Kong,‡[a] Mengting Fan,‡[a] Zewen Zhang,[a] Lei Wang,[a] Renpeng Chen,[a] Yi Hu,[a] Jing Ma *[a] and Zhong Jin *[ab]

Received 3rd July 2019
Accepted 14th August 2019

DOI: 10.1039/c9ta07127j

rsc.li/materials-a

Selenium sulfides are considered attractive cathode materials for lithium storage due to their higher specific capacities than elemental selenium and better electrical conductivity than sulfur. However, due to the dissolution of intermediate polyselenides and polysulfides, selenium sulfides suffer from fast capacity degradation and low coulombic efficiency. Herein, we report a chelation competition induced polymerization (CCIP) strategy for the synthesis of multi-yolk–shell Co_4N@carbon (MYS-Co_4N@C) nanoboxes as an advanced SeS_2 host material, which can simultaneously achieve good rate capability and cycling stability. Due to both physical confinement by carbon shells and strong chemical affinity of polar Co_4N yolks, the MYS-Co_4N@C nanoboxes can restrict the outward diffusion of S_x^{2-} and Se_x^{2-} intermediates to suppress self-discharge and boost cycling stability. Benefitting from the high metallic conductivity and catalytic activity of Co_4N, the SeS_2-filled MYS-Co_4N@C composite cathode also shows good electron/ion transport properties, and thus the redox kinetics and utilization ratio of the SeS_2 active material can be improved. As a result, a high specific capacity retention and a superior rate capability can be achieved at a high SeS_2 loading content of 70 wt%. When the mass loading of SeS_2 is increased to 4.5 mg cm^{-2}, the composite cathode still exhibits high reversible capacity and stable cycle performance.

Introduction

Rechargeable lithium–sulfur batteries are considered a promising candidate for next-generation energy-storage devices because of their high theoretical energy density, environmental friendliness, and low cost.[1–3] So far, tremendous efforts have been devoted to the design of key components for Li–S batteries, such as electrolyte additives,[4,5] modified separators,[6–9] functional binders,[10–12] and host materials.[13–16] Benefiting from these efforts, the cycle life and specific capacity of Li–S batteries have been significantly improved in recent years.[17–23] Nevertheless, the practical application of Li–S batteries is still hindered by the low active material utilization ratio resulting from the intrinsic low conductivity of S and Li_2S.[24,25] Therefore, an alternative conductive cathode material should be developed to solve the inherent problems of the sulfur cathode. Selenium (Se) has aroused considerable attention due to its significantly higher room-temperature electrical conductivity (1×10^{-3} S m^{-1}) compared to sulfur (5×10^{-28} S m^{-1}),[26,27] giving rise to a higher utilization rate and better reaction kinetics. However, the fast capacity decay and self-discharge of Li–Se batteries caused by the shuttle effect of polyselenides (Se_x^{2-}) are still obstacles to realizing practical applications.[28]

To overcome the above-mentioned drawbacks of pristine elemental S and Se, a class of selenium–sulfur solid solutions (Se_xS_y) has been explored as promising cathode materials for rechargeable batteries.[27,29,30] In pioneering work by Amine's group, Se_xS_y-based cathodes were adopted to achieve lithium and sodium storage, benefiting from their higher conductivity compared to elemental S and higher energy density compared to elemental Se.[27,31] However, similar to sulfur cathodes, SeS_2-based cathodes also suffer from poor cycle life and low coulombic efficiency because of the dissolution and shuttling of polar reaction intermediates.[32,33] Recently, some polar nanomaterials, such as metal oxides,[34–38] sulfides,[39–42] and nitrides,[43–45] have been utilized as novel adsorbents to replace nonpolar carbon host materials, because their strong interactions with polysulfides can suppress the shuttle effect and improve the cycle stability. Nevertheless, most metal oxides have inherently low electrical conductivity, which impedes electron transport and high sulfur utilization. Therefore, metal nitrides/sulfides with high electrical conductivity can be regarded as better choices for the SeS_2 hosts.[41–44] Among transition metal nitrides, cobalt nitride (Co_4N) can facilitate fast electron

[a]Key Laboratory of Mesoscopic Chemistry of MOE, Jiangsu Key Laboratory of Advanced Organic Materials, School of Chemistry and Chemical Engineering, Nanjing University, Nanjing 210023, China. E-mail: majing@nju.edu.cn; zhongjin@nju.edu.cn

[b]Shenzhen Research Institute of Nanjing University, Shenzhen 518063, China

† Electronic supplementary information (ESI) available. See DOI: 10.1039/c9ta07127j

‡ T. Chen, W. Kong and M. Fan contributed equally to this work.

transfer and kinetically enhance the redox reactions, owing to its high electrical conductivity (1.67×10^5 S m^{-1}) and bifunctional catalytic properties.[45,46] Following this line of thought, it is suggested that the construction of hybrid host materials composed of polar nanomaterials and highly conductive carbon is a feasible approach to synergistically resolve the shuttling issues of polysulfides and polyselenides. Furthermore, an ideal nanostructural SeS_2 host should also possess the following advantageous features: (i) large void spaces for encapsulating a high content of SeS_2 species and tolerating volumetric expansion; (ii) sufficient adsorption and catalytic sites for accelerated redox reaction kinetics and subsequent reversible utilization of SeS_2 species.

To satisfy the above requirements, here we exploit a chelation competition induced polymerization (CCIP) strategy for the preparation of multi-yolk–shell Co_4N@carbon (MYS-Co_4N@C) nanoboxes to greatly enhance the overall performance of Li–SeS_2 batteries. In this unique multi-yolk–shell nanostructure, polar Co_4N can restrict the outward diffusion of polysulfides and polyselenides through strong chemical affinity and also exhibit good electrocatalytic properties for improving the redox reaction kinetics. The carbon outer shell functions as a submicron-sized reaction chamber and provides physical confinement for polysulfides/polyselenides. Moreover, the highly conductive Co_4N yolks and carbon layers can ensure smooth electron transport and a high utilization ratio of active materials during the discharge/charge process. As a result, the MYS-Co_4N@C/SeS_2 cathode exhibited high specific capacity, improved rate capability and good cycling stability. With a high SeS_2 loading of 4.5 mg cm^{-2}, the MYS-Co_4N@C/SeS_2 cathode also displayed high areal capacities and superior cycling stability. More importantly, the Li–SeS_2 batteries based on the MYS-Co_4N@C/SeS_2 cathode showed remarkable self-discharge suppression performance, owing to the good trapping capability for polysulfides and polyselenides to inhibit the shuttle effect.

Experimental

Synthesis of zeolitic imidazolate framework-67 (ZIF-67) nanocubes

Briefly, 5 mg of CTAB was first mixed/dissolved with 10 mL of a $Co(NO_3)_2 \cdot 6H_2O$ aqueous solution. In another beaker, 4.54 g of 2-methylimidazole was added into 70 mL of deionized water. Then, these two solutions were mixed quickly and stirred vigorously for 20 min at room temperature. The purple product was collected by centrifugation at 6000 rpm for 5 min, washed with deionized water and ethanol several times, and dried at 80 °C in an oven overnight.

Synthesis of yolk–shell-ZIF-67@polydopamine (YS-ZIF-67@PDA) nanoboxes

The obtained ZIF-67 nanocubes were dispersed in 75 mL of methanol. Then, 15 mL of a 20 mM dopamine methanol solution was added into the above solution and the mixed solution was stirred for 5 min at room temperature. After that, the mixture was stirred continuously at 55 °C for 3 h. The black powder was collected by centrifugation at 4000 rpm for 10 min, washed with methanol several times and dried at 80 °C overnight.

Synthesis of MYS-Co_4N@C nanoboxes

The as-obtained YS-ZIF-67@PDA nanoboxes were placed in a porcelain boat and annealed in a tube furnace at 500 °C for 4 h under a mixed atmosphere of Ar/NH_3 (50 : 50) with a heating rate of 1 °C min^{-1}. After cooling down, the MYS-Co_4N@C nanoboxes were obtained.

Synthesis of carbon nanoboxes (C-NBs) as a control sample

For comparison, C-NBs were also prepared using the same method as for MYS-Co_4N@C nanoboxes, but the reaction time was prolonged. After the addition of the dopamine methanol solution into the methanol suspension of ZIF-67, the mixture was stirred continuously at 55 °C for 7 h. The as-prepared hollow PDA nanoboxes (as shown in Fig. S3d†) were collected by centrifugation, washed with methanol and dried at 80 °C overnight. Then, the hollow PDA nanoboxes were thermally annealed at 500 °C for 4 h in a mixed atmosphere of Ar/NH_3 (50 : 50) with a heating rate of 1 °C min^{-1}. After cooling down to room temperature, the C-NB control sample was obtained.

Synthesis of MYS-Co_4N@C/SeS_2 and C-NBs/SeS_2 composites

Typically, MYS-Co_4N@C nanoboxes and SeS_2 were mixed in a weight ratio of 3 : 7. Then, the mixture was sealed in a glass vial and heated at 180 °C for 12 h to obtain the MYS-Co_4N@C/SeS_2 composite. The control sample, the C-NBs/SeS_2 composite, was prepared by the same method using C-NBs as the SeS_2 host instead of MYS-Co_4N@C nanoboxes.

Adsorption experiments of Li_2S_4

The Li_2S_4 solution (5 mM) was prepared by mixing sulfur powder and lithium sulfide (Li_2S) with a molar ratio of 3 : 1 in a mixed solvent of 1,3-dioxolane/1,2-dimethoxyethane (DOL/DME, 1 : 1 by volume) followed by continuous stirring at room temperature for 24 h. Then, 30 mg of the MYS-Co_4N@C powder was soaked into the Li_2S_4 solution (5 mL) in an Ar-filled glovebox. The resultant MYS-Co_4N@C/Li_2S_4 composite was collected by centrifugation and dried in a vacuum oven.

Characterization

The morphologies and structures of the samples were characterized using a field-emission scanning electron microscope (FE-SEM, FEI Nova NanoSEM 450, accelerating voltage: 10 kV) equipped with a Bruker energy-dispersive X-ray spectroscope (EDX) for elemental mapping analysis. Nitrogen sorption isotherms and the BET surface area were measured with a Quantachrome Autosorb-IQ-2C analyzer at 77 K. TGA analysis was performed using a NETZSCH-STA-449C instrument in a N_2 atmosphere from 50 to 600 °C at a heating rate of 10 °C min^{-1}. Powder XRD patterns were measured on a Shimadzu 6000 X-ray diffractometer with Cu Kα radiation (λ = 1.5406 Å). X-ray

photoelectron spectra (XPS) were measured on a PHI-5000 VersaProbe X-ray photoelectron spectrometer with Al Kα X-ray radiation.

Electrochemical measurements

To fabricate the working electrode, 80 wt% of the MYS-Co_4N@C/SeS_2 composite, 10 wt% of KJ-black (EC600J), and 10 wt% of polyvinylidenefluoride (PVDF) were dispersed in *N*-methylpyrrolidone (NMP). The homogeneous slurry was spread onto Al foil and dried at 55 °C for 24 h in a vacuum. The areal mass loading of SeS_2 is controlled to 1.2 mg cm^{-2} or 4.5 mg cm^{-2} (for high mass loading tests). The electrode film was roll-pressed and cut into round disks with a diameter of 12 mm. CR 2032 coin cells were assembled in an Ar-filled glove box using Li foil as the counter electrode and a Celgard 2400 membrane as the separator. The electrolyte was composed of 1 M lithium bis(trifluoromethanesulfonyl)imide (LiTFSI) dissolved in a mixture of 1,3-dioxolane (DOL) and dimethoxymethane (DME) (1 : 1 by volume). For the normal cathode, 30 μL of the electrolyte was used, and approximately 70 μL of the electrolyte was used for the high-loading cathode. Galvanostatic charge–discharge measurements were performed on a battery test system (LAND CT2001A, Wuhan) with cut-off voltages of 1.8–2.8 V. Cyclic voltammetry (CV) studies were conducted on a Chenhua CHI-760 electrochemical workstation at a sweeping rate of 0.5 mV s^{-1} in the voltage range of 1.8–2.8 V (*vs.* Li/Li^+).

Self-discharge tests

The self-discharge rate (η%) was calculated using the following equations:

$$\eta\% = (C_{\mathrm{discharge}(N)} - C_{\mathrm{charge}(N-1)})/C_{\mathrm{charge}(N-1)} \times 100\%, \text{ or}$$

$$\eta\% = (C_{\mathrm{discharge}(N-1)} - C_{\mathrm{discharge}(N)})/C_{\mathrm{discharge}(N-1)} \times 100\%$$

where $C_{\mathrm{charge}(N-1)}$ is the charge capacity of the $(N-1)^{\mathrm{th}}$ cycle (N = 6 or 11) and $C_{\mathrm{discharge}(N)}$ is the discharge capacity of the N^{th} cycle.

Results and discussion

Synthesis and characterization

Fig. 1a shows the synthesis procedure of the MYS-Co_4N@C/SeS_2 composite. First, regular ZIF-67 nanocubes were prepared by the reaction of Co^{2+} ions and 2-methylimidazole (2-MIL) monomers *via* a previous method.[47] Second, YS-ZIF-67@PDA nanoboxes were formed by reaction with dopamine in methanol for 3 h. We suggest that this hollowing process could be interpreted as a CCIP mechanism. Briefly, owing to the stronger chelation interaction of Co^{2+} ions with dopamine than with 2-MIL monomers, after the introduction of dopamine, the Co^{2+} ions in ZIF-67 nanocubes were gradually released and then the ZIF-67 nanocubes were partially disassembled to form YS-ZIF-67 nanoboxes. Meanwhile, the released 2-MIL monomers triggered the polymerization of dopamine,[48] thus leading to the formation of YS-ZIF-67@PDA nanoboxes. Then, the YS-ZIF-67@PDA nanoboxes were converted to MYS-Co_4N@C nanoboxes through a subsequent thermal treatment in an NH_3 atmosphere. In this step, the inner Co_4N yolks were prepared by the thermal nitridization treatment of ZIF-67 yolks in an NH_3 atmosphere, and the carbon outer shell was derived from the thermal pyrolysis of PDA. Finally, SeS_2 was filled into the void space of MYS-Co_4N@C nanoboxes by a modified melt-diffusion method to obtain the MYS-Co_4N@C/SeS_2 composite.[13]

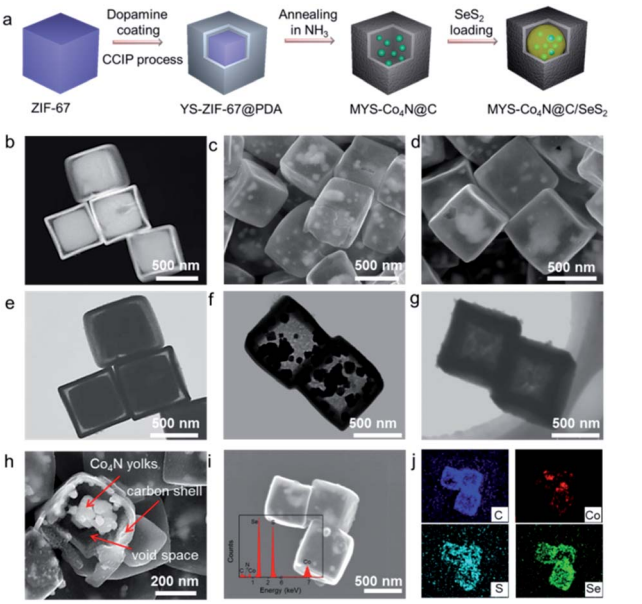

Fig. 1 (a) Schematic illustration of the synthetic procedure of the MYS-Co_4N@C/SeS_2 composite. (b–d) SEM and (e–g) TEM images of (b and e) YS-ZIF-67@PDA nanoboxes, (c and f) MYS-Co_4N@C nanoboxes, and (d and g) the MYS-Co_4N@C/SeS_2 composite. (h) SEM image of cracked MYS-Co_4N@C nanoboxes and (i) SEM image (the inset is the EDX spectrum of the MYS-Co_4N@C/SeS_2 composite) and (j) the corresponding elemental maps of the MYS-Co_4N@C/SeS_2 composite.

Scanning electron microscopy (SEM) and transmission electron microscopy (TEM) were conducted to characterize the morphological features of the samples. The as-prepared ZIF-67 nanocubes are highly uniform with an average size of about 400 nm (Fig. S1†). After the dopamine coating and the CCIP reaction process, the yolk–shell structures of YS-ZIF-67@PDA nanoboxes were formed, which could be clearly identified from the visible interlayer voids between the PDA outer shells and the inner ZIF-67 yolks (Fig. 1b and e). X-ray diffraction (XRD) analysis revealed that the YS-ZIF-67@PDA nanoboxes have a similar crystalline phase to ZIF-67 nanocubes (Fig. S2†). The size of the inner ZIF-67 yolks could be precisely adjusted by variation of reaction time. As revealed by the TEM characterization in Fig. S3,† when the reaction time was increased from 30 min to 5 h, the size of the inner ZIF-67 yolks decreased from about 360 nm to 180 nm (Fig. S3a–c†). If the reaction was processed for 7 h, the inner ZIF-67 yolks would be completely removed, and hollow PDA nanoboxes would be produced (Fig. S3d†). After the thermal treatment in NH_3 gas, the inner ZIF-67 yolks were converted into small Co_4N nanocrystals, generating large void spaces in the resultant MYS-Co_4N@C nanoboxes (Fig. 1c and f). With the formation of carbon shells

by the pyrolysis of the PDA outer layer, the regular cubic morphology was well preserved, as shown in Fig. 1c. The inner void space in MYS-Co_4N@C nanoboxes can be observed between the carbon outer shell and the inner Co_4N yolks, as clearly shown in a cracked nanobox (Fig. 1h). The thickness of the carbon outer shell is about 15 nm, and the size of Co_4N yolks is around 20–50 nm (Fig. 1f). After the filling with SeS_2 by the melt-diffusion method, the resultant MYS-Co_4N@C/SeS_2 composite maintained the original cubic morphology well, and no sulfur particles were observed outside the surface (Fig. 1d). TEM observation confirmed that SeS_2 was successfully encapsulated into the inner void space of MYS-Co_4N@C nanoboxes (Fig. 1g). The energy-dispersive X-ray spectrum (EDX) clearly showed the presence of Co, C, Se and S elements, indicating a large content of SeS_2 in the MYS-Co_4N@C/SeS_2 composite (the inset in Fig. 1i). The corresponding elemental mapping images further revealed the uniform distribution of SeS_2 in the MYS-Co_4N@C nanoboxes (Fig. 1i and j).

Fig. 2a displays the XRD patterns of SeS_2, MYS-Co_4N@C nanoboxes, and the MYS-Co_4N@C/SeS_2 composite. The diffraction peaks of ZIF-67 crystals (Fig. S2†) disappeared in the XRD pattern of MYS-Co_4N@C nanoboxes, and three main diffraction peaks at 44.1°, 51.2°, and 75.4° can be ascribed to the (111), (220) and (222) lattice planes of cubic phase Co_4N (JCPDS card No. 01-1259).[49] This indicates that the inner ZIF-67 yolks were completely converted to Co_4N nanocrystals after annealing in an NH_3 atmosphere. The broad characteristic peak around 24.2° is assigned to the (002) planes of partially graphitic layers in the carbon outer shell. The characteristic diffraction peaks in the XRD pattern of the MYS-Co_4N@C/SeS_2 composite confirm the presence of SeS_2. Thermogravimetric analysis (TGA) was conducted to determine the weight ratio of Co_4N in MYS-Co_4N@C nanoboxes. The mass content of Co_4N was determined to be about 34.9 wt%, and the weight ratio of carbon was around 65.1 wt%, as detailed in Fig. S4.† The mass content of SeS_2 in the MYS-Co_4N@C/SeS_2 composite was also measured to be around 70 wt% (Fig. 2b). The N_2 absorption–desorption isotherms and Barrett–Joyner–Halenda pore size distributions of MYS-Co_4N@C nanoboxes and the MYS-Co_4N@C/SeS_2 composite are shown in Fig. 2c and d, respectively. The MYS-Co_4N@C nanoboxes show a relatively large Brunauer–Emmett–Teller (BET) surface area of 142 $m^2\ g^{-1}$ and a pore volume of 1.05 $cm^3\ g^{-1}$, which could offer sufficient inner space for accommodating a large weight content of SeS_2. After the encapsulation of SeS_2, the BET surface area and pore volume of the MYS-Co_4N@C/SeS_2 composite sharply decreased to 25 $m^2\ g^{-1}$ and 0.12 $cm^3\ g^{-1}$, respectively, indicating the successful filling of SeS_2. As a control sample, C-NBs without Co_4N yolks were also prepared using the same method, but the reaction time of the CCIP reaction process in dopamine solution was prolonged to 7 h (as detailed in the ESI†). Clearly, the ZIF-67 yolks were fully removed after the long-term reaction with dopamine and thermal treatment in an NH_3 atmosphere, as shown in Fig. S3d and S5.† The performance comparison of MYS-Co_4N@C/SeS_2 and SeS_2-filled C-NB (C-NBs/SeS_2) composites is expected to be helpful to understand the enhancement effect of Co_4N yolks on battery performances.

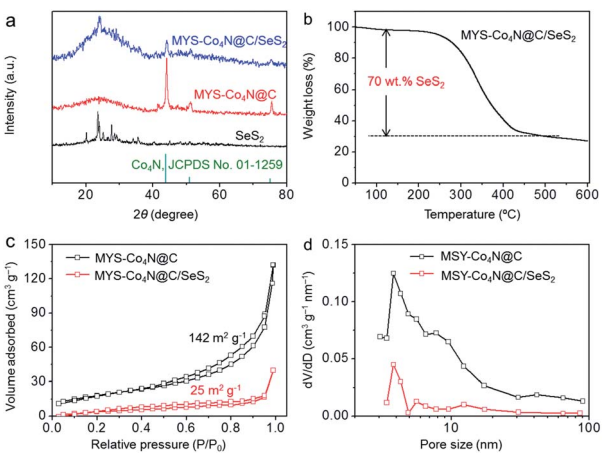

Fig. 2 (a) XRD patterns of SeS_2, MYS-Co_4N@C nanoboxes, and the MYS-Co_4N@C/SeS_2 composite. (b) TGA curve of the MYS-Co_4N@C/SeS_2 composite under a nitrogen atmosphere. (c) Nitrogen adsorption–desorption isotherms and (d) pore-size distributions of MYS-Co_4N@C nanoboxes and the MYS-Co_4N@C/SeS_2 composite.

Electrochemical properties

Cyclic voltammetry (CV) was utilized to study the catalysis effect and electrochemical reaction kinetics of the MYS-Co_4N@C/SeS_2 composite and C-NBs/SeS_2 control sample by comparing the peak potentials and onset potentials of reduction peaks and oxidation peaks (Fig. 3a and b). The peak potentials of two reduction peaks in the CV curves of the MYS-Co_4N@C/SeS_2 electrode are higher than those of C-NBs/SeS_2 electrode, and the peak potential of the single oxidation peak is lower, indicating that the presence of Co_4N can reduce the electrochemical polarization (Fig. 3c). Moreover, the onset potentials of reduction and oxidation peaks are also analyzed, which is defined as the potential at which 10% of the maximum current value at the peak potential was reached.[50,51] As shown in Fig. 3d, the MYS-Co_4N@C/SeS_2 electrode shows a higher onset potential of reduction peaks and lower onset potential of the oxidation peak than the C-NBs/SeS_2 electrode, indicating that the good electrocatalytic activity of Co_4N can improve the redox reaction kinetics. These results confirm that the polar and conductive Co_4N yolks can reduce the electrochemical polarization and accelerate the redox kinetics in Li–SeS_2 batteries.

To visually evaluate the chemisorption ability of Co_4N yolks to S_x^{2-} and Se_x^{2-} species, the coin cells of Li–SeS_2 batteries based on MYS-Co_4N@C/SeS_2 and C-NBs/SeS_2 electrodes were disassembled in an Ar-filled glovebox at the fully discharged state after 50 cycles at 0.2C. The electrodes were separately immersed into a mixture of 1,3-dioxolane (DOL) and 1,2-dimethoxyethane (DME) (1 : 1 by volume) for 2 h. As shown in Fig. 3e, the mixed solvent with the soaked MYS-Co_4N@C/SeS_2 electrode remained very light color. In contrast, the mixture with the immersed C-NBs/SeS_2 electrode turned to a dark yellow, indicating the dissolution of polysulfides/polyselenides into the organic electrolyte. This result suggests that the MYS-Co_4N@C

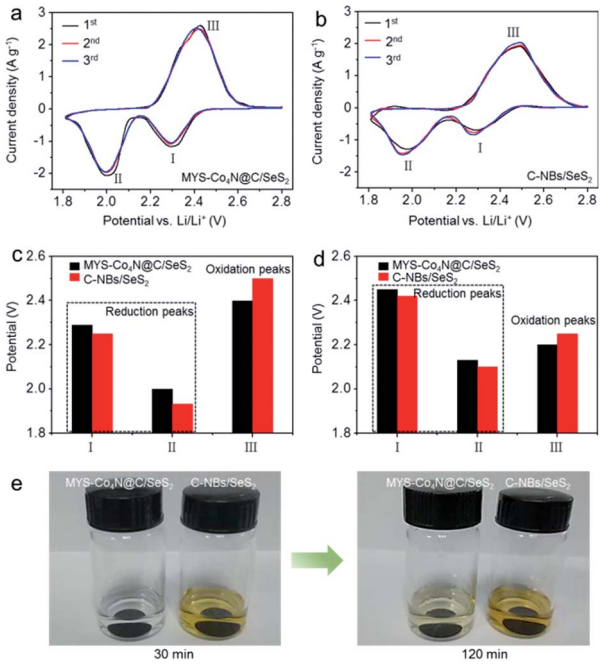

Fig. 3 CV profiles of (a) MYS-Co_4N@C/SeS_2 and (b) C-NBs/SeS_2 electrodes in the potential range from 1.8 to 2.8 V at a scanning rate of 0.5 mV s^{-1}. (c) Corresponding peak potentials and (d) onset potentials of MYS-Co_4N@C/SeS_2 and C-NBs/SeS_2 electrodes measured during the 2nd CV cycle in (a) and (b), respectively. (e) Visual comparison of MYS-Co_4N@C/$SeSe_2$ and C-NBs/SeS_2 electrodes immersed in mixed DOL/DME solutions at the fully discharged state after 50 cycles at 0.2C, respectively.

host can effectively suppress the outward diffusion of dissolved S_x^{2-} and Se_x^{2-}, originating from both the chemical adsorption to polar Co_4N yolks and the physical confinement by carbon shells.

To verify the chemical interactions between polar Co_4N and polysulfides, Li_2S_4 was chosen as a representative prototype of polysulfides. X-ray photoelectron spectroscopy (XPS) was conducted to study the chemical composition of MYS-Co_4N@C nanoboxes before and after adsorbing Li_2S_4 (the details are described in the Experimental section of the ESI†). Fig. S6a† shows the XPS spectra at the Co $2p_{3/2}$ region of MYS-Co_4N@C nanoboxes, in which the Co $2p_{3/2}$ band can be deconvoluted into two characteristic peaks at 778.3 and 780.3 eV. The peaks at 778.3 eV could be indexed to the Co(0) species, and the peak at 780.3 eV was attributed to the Co–N bond in the composite.[38] After the adsorption of Li_2S_4 (Fig. S6b†), the MYS-Co_4N@C/Li_2S_4 composite shows an additional peak located at 778.9 eV, confirming the formation of Co–S bonds. The XPS results suggest that the Co_4N yolks can chemically bind with polysulfides through Co–S bonds.[52] Moreover, the peak intensity of Co(0) species was significantly reduced, indicating the chemical interaction of Co(0) with S_4^{2-} species. Since polyselenides have similar physicochemical properties and shuttling issues to polysulfides, it can be reasonably deduced that the Co_4N yolks in MYS-Co_4N@C can effectively restrict the diffusion of polysulfides and polyselenides by strong chemical interactions.

To further investigate the electrochemical properties of the MYS-Co_4N@C host for storing polysulfides/polyselenides, galvanostatic discharge/charge tests of the MYS-Co_4N@C/SeS_2 electrode were conducted at 0.1C (based on the loading weight of SeS_2, 1.0C = 1123 mA g^{-1}). As shown in Fig. 4a, typical discharge/charge curves of the MYS-Co_4N@C/SeS_2 electrode show four discharge plateaus. The first two discharge plateaus located at 2.30 V and 2.14 V originated from the conversion of SeS_2 to soluble long-chain polysulfides and polyselenides, respectively. In the subsequent discharge process, the two plateaus observed at 2.10 and 2.05 V were ascribed to the transformation of long-chain polysulfides and polyselenides to insoluble short-chain polysulfides and polyselenides. The initial discharge and charge capacities of the MYS-Co_4N@C/SeS_2 electrode were 1015 and 998 mA h g^{-1}, respectively, corresponding to a coulombic efficiency of 95%, which indicates the high utilization ratio of SeS_2. The potential hysteresis between the discharge and charge plateaus of the MYS-Co_4N@C/SeS_2 electrode is much lower than that of the C-NBs/SeS_2 electrode, implying better redox kinetics of polysulfides and polyselenides in the MYS-Co_4N@C host. The cycling performances of MYS-Co_4N@C/SeS_2 and C-NBs/SeS_2 electrodes were compared at a current density of 0.2C, as shown in Fig. 4b. Without the presence of polar Co_4N yolks, the C-NB/SeS_2 cathode suffered from severe capacity fading with a low capacity of 600 mA h g^{-1} after 100 cycles, with only 52% retention of the initial discharge capacity. In comparison, the MYS-Co_4N@C/SeS_2 cathode

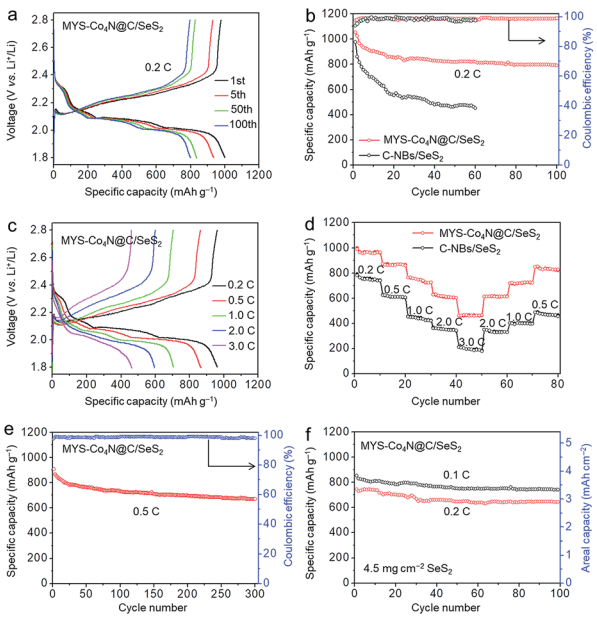

Fig. 4 (a) Discharge/charge profiles of the MYS-Co_4N@C/SeS_2 cathode at 0.2C. (b) Cycle performances of MYS-Co_4N@C/SeS_2 and C-NBs/SeS_2 cathodes at 0.2C. (c) Discharge/charge profiles of the MYS-Co_4N@C/SeS_2 cathode at various current rates. (d) Rate capability comparison of MYS-Co_4N@C/SeS_2 and C-NBs/SeS_2 cathodes. (e) Cycle stability of the MYS-Co_4N@C/SeS_2 cathode at 0.5C. (f) Cycling performances and corresponding areal capacities of the MYS-Co_4N@C/SeS_2 cathode with a high sulfur loading of 4.5 mg cm^{-2} at 0.1 and 0.2C, respectively.

exhibited a much higher discharge capacity of 996 mA h g^{-1} after 100 cycles, corresponding to a capacity retention as high as 85%. The cycling stability of the MYS-Co_4N@C/SeS_2 electrode is far superior to that of the C-NBs/SeS_2 electrode, confirming the structural advantages of the MYS-Co_4N@C host in trapping polysulfides/polyselenides. In addition, the coulombic efficiency of the MYS-Co_4N@C/SeS_2 electrode was more than 99% during the long-term cycling process. These results demonstrate that the rationally designed MYS-Co_4N@C host can effectively mitigate the dissolution of polysulfides/polyselenides into the electrolyte and improve the cycling life.

The MYS-Co_4N@C host also showed great improvement towards the rate performance of Li–SeS_2 batteries, as displayed in Fig. 4c and d. When the rate was increased from 0.2C to 3.0C, the reversible discharge capacities of the MYS-Co_4N@C/SeS_2 electrode gradually decreased from 962, 866, 735, and 610 to 460 mA h g^{-1} at 0.2, 0.5, 1.0, 2.0, and 3.0C, respectively. When the current density was switched back to 0.2C, the discharge capacity recovered to 838 mA h g^{-1}, indicating the good structural integrity and reaction kinetics at a high rate. In contrast, the C-NBs/SeS_2 electrode exhibited much lower discharge capacities of 753 mA h g^{-1} at 0.2C, 609 mA h g^{-1} at 0.5C, 434 mA h g^{-1} at 1.0C, 355 mA h g^{-1} at 2.0C, and 206 mA h g^{-1} at 3.0C (Fig. 4d), which may be attributed to the insufficient confinement of polysulfides/polyselenides in the C-NB host. These results further confirm that the efficient adsorption of polysulfides/polyselenides and good conductivity of the MYS-Co_4N@C/SeS_2 cathode can enhance the redox reaction kinetics and facilitate fast electron/ion transport. The long-term cycling performance of the MYS-Co_4N@C/SeS_2 electrode was tested at 0.5C for 300 cycles (Fig. 4e). The MYS-Co_4N@C/SeS_2 electrode delivered an initial discharge capacity of 909 mA h g^{-1} and retained a reversible capacity of 669 mA h g^{-1} after 300 cycles. The capacity decay was estimated to be ~0.088% per cycle with an average coulombic efficiency of above 99%.

To realize a higher areal capacity of Li–SeS_2 batteries for practical applications, MYS-Co_4N@C/SeS_2 cathodes with ultra-high areal SeS_2 loading were also fabricated by increasing the thickness of the electrode film. Good cycling stability was achieved with the thick MYS-Co_4N@C/SeS_2 electrode with an areal SeS_2 loading of 4.5 mg cm^{-2} over 100 cycles at 0.1 and 0.2C (Fig. 4f). At such a high areal loading, the MYS-Co_4N@C/SeS_2 electrode still delivered an initial specific capacity of 850 mA h g^{-1} at 0.1C (corresponding to 3.82 mA h cm^{-2} at 0.66 mA cm^{-2}) and 745 mA h g^{-1} at 0.2C (3.35 mA h cm^{-2} at 1.3 mA cm^{-2}). After 100 cycles, the thick electrode still exhibited high reversible capacities of 739 (3.33 mA h cm^{-2}) and 641 mA h g^{-1} (2.89 mA h cm^{-2}) at 0.1 and 0.2C, respectively, indicating the high capacities and well-preserved cycling stability under a high areal loading of SeS_2. Compared to other Se_xS_y based cathodes in previous reports (Table S1†),[33,53–57] the MYS-Co_4N@C/SeS_2 cathode exhibited a very competitive cycling stability. The good electrochemical performances of the MYS-Co_4N@C/SeS_2 cathode should be attributed to the following merits. First, numerous Co_4N yolks provide adequate chemisorption sites to immobilize polysulfides and polyselenides, thereby effectively reducing the shuttle effect. Second, Co_4N yolks have apparent electrocatalytic activity for accelerated redox kinetics of polysulfides/polyselenides. Third, the high conductivity of Co_4N yolks and carbon shells can facilitate electron/ion transfer and promote the reversible redox conversion of SeS_2 during discharge/charge processes.

To further investigate the composition variation of the MYS-Co_4N@C/SeS_2 electrode after long-term cycling, the cell was disassembled after cycling 300 times at 0.5C and the electrode film was characterized by the XRD method. The XRD patterns before and after cycling exhibited no obvious change (Fig. S7†), indicating the highly reversible conversion of SeS_2 and good electrochemical stability of the MYS-Co_4N@C/SeS_2 electrode. The SEM images (Fig. S8a†) showed that the cubic morphology of the MYS-Co_4N@C/SeS_2 composite after long-term cycling had almost no change, indicating the good structural integrity of the MYS-Co_4N@C host. Only minimal polysulfides/polyselenides were observed on the surface of the MYS-Co_4N@C/SeS_2 electrode after cycling, which was distinct from the C-NBs/SeS_2 electrode (Fig. S8b†), implying more effective confinement of polysulfides/polyselenides in the MYS-Co_4N@C/SeS_2 electrode. Moreover, EDX elemental maps also revealed that SeS_2 was still evenly distributed in the MYS-Co_4N@C host after cycling (Fig. S9†).

Similar to Li–S batteries, Li–SeS_2 batteries also seriously suffer from the self-discharge issue, which is attributed to the dissolution of intermediate polysulfides/polyselenides into the electrolyte. The self-discharge behaviors of Li–SeS_2 batteries with MYS-Co_4N@C/SeS_2 and C-NBs/SeS_2 cathodes were compared at different states of charge. Fig. 5a and b display the discharge/charge profiles of Li–SeS_2 batteries with MYS-Co_4N@C/SeS_2 and C-NBs/SeS_2 cathodes at fully discharged states, respectively. After being fully discharged to 1.8 V in the 10th cycle, the batteries were rested for 96 h and then charged/discharged again. After resting for 96 h, the Li–SeS_2 cell with the MYS-Co_4N@C/SeS_2 cathode displayed a self-discharge ratio of only 7.2%, which was much lower than that with the C-NB/SeS_2 cathode (which exhibited a self-discharge ratio of 20.5%). Furthermore, the Li–SeS_2 cells were also investigated at partially charged states (Fig. 5c and d). Briefly, the cells were partially charged to 2.3 V in the 5th cycle and rested for 48 h, and then further cycled. After partially charging to 2.3 V and resting for 48 h, the Li–SeS_2 cell with the MYS-Co_4N@C/SeS_2 cathode exhibited a self-discharge ratio of only 9.4%. In contrast, a self-discharge ratio of 22.9% after resting was observed for the cells with the C-NB/SeS_2 cathode. These results further suggest the effectiveness of the multi-yolk–shell structure and polar Co_4N yolks for trapping soluble polysulfides/polyselenides (Fig. 5e). The low self-discharge of the MYS-Co_4N@C/SeS_2 cathode should be ascribed to the strong chemisorption by polar Co_4N yolks.

DFT calculation

To reveal the interaction mechanism of polyselenides/polysulfides with Co_4N, density functional theory (DFT) simulation was further performed. Fig. 6 and S10† show the optimized adsorption configurations with the corresponding adsorption energies of Li_2S_n and Li_2Se_n (n = 4, 6, 8) on Co_4N (111), respectively. Based on the simulation results (Table S2†),

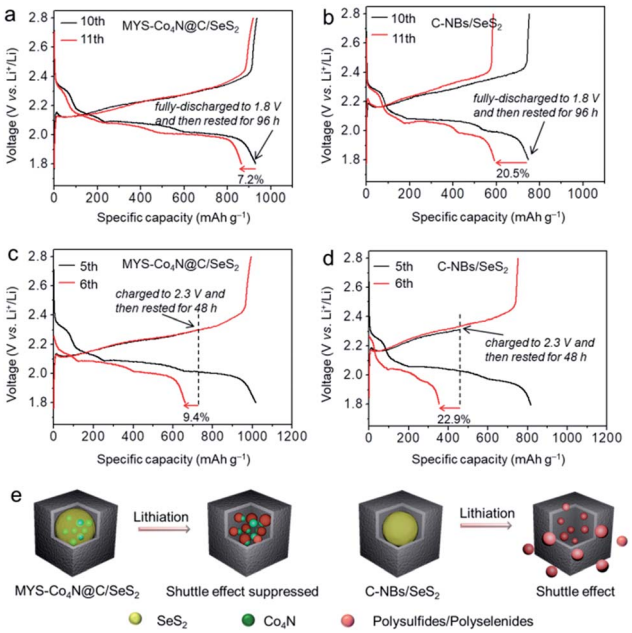

Fig. 5 Self-discharge evaluation of Li–SeS_2 batteries based on (a and c) MYS-Co_4N@C/SeS_2 and (b and d) C-NB/SeS_2 cathodes in different discharge and charge states at 0.2C. (a and b) The Li–SeS_2 batteries were fully discharged to 1.8 V in the 10th cycle and rested for 96 h, and then further cycled again. (c and d) The Li–SeS_2 batteries were partially charged to 2.3 V in the 5th cycle and rested for 48 h, and then further cycled again. (e) Schematic illustration of the structural advantages of MYS-Co_4N@C/SeS_2 over C-NBs/SeS_2 for the confinement of polysulfides/polyselenides and the suppression of the shuttle effect, due to the presence of numerous polar Co_4N yolks inside the void space of nanoboxes.

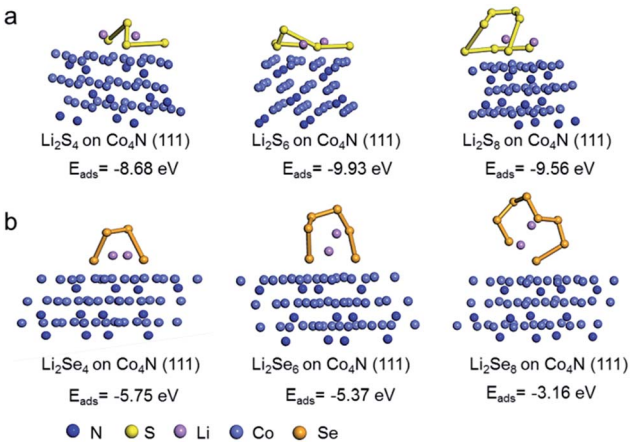

Fig. 6 DFT calculation results of the adsorption geometric configurations and the calculated adsorption energies of (a) Li_2S_n and (b) Li_2Se_n (n = 4, 6, 8) with the (111) planes of Co_4N.

the adsorption energies of Li_2S_8, Li_2S_6 and Li_2S_4 on Co_4N are calculated to be −8.68, −9.93 and −9.56 eV, respectively, indicating the strong affinity between Co_4N and Li_2S_n (n = 4, 6, 8). The theoretical calculation results hint that the polysulfides and polyselenides tend to be well trapped when Co_4N is present, and thus the shuttle issue was efficiently inhibited. In addition, we also calculated the adsorption energies of Li_2Se_n (n = 4, 6, 8) on Co_4N (111), which are much lower than those of Li_2S_n (n = 4, 6, 8). Compared with polar Co_4N, nonpolar graphene displays a much lower adsorption ability for polar polysulfides/polyselenides (Fig. S11 and Table S3†). These theoretical results also reveal that polar Co_4N nanoparticles exhibit strong affinity to polysulfide and polyselenide species, thus resulting in boosted electrochemical performance.

Conclusions

In summary, we have rationally designed and prepared a hollow and multi-yolk–shell structured composite *via* a CCIP strategy as a highly efficient host for the storage of SeS_2. The experimental results reveal that the numerous polar Co_4N yolks provide a strong adsorption force for inhibiting the outward diffusion of polysulfides/polyselenides and also exhibit obvious electrocatalytic activity for improving the redox kinetics of SeS_2. The carbon shell functions as a nanoscale reaction chamber to physically accommodate polar polysulfides/polyselenides. Moreover, the highly conductive Co_4N yolks and carbon shell ensure smooth electron transport and facilitate reversible conversion of polysulfides/polyselenides during cycling. Benefiting from these merits, the MYS-Co_4N@C/SeS_2 composite cathodes exhibit high capacity, a long cycling life and good self-discharge suppression in Li–SeS_2 batteries. We expect that this work may open up the possibility of rationally designing advanced nanostructured electrode materials for high-performance Li–Se_xS_y batteries.

Conflicts of interest

The authors declare no competing financial interest.

Acknowledgements

This work was supported by the National Key R&D Program of China (2017YFA0208200, 2016YFB0700600, and 2015CB659300), Projects of the NSFC (21872069, 51761135104, and 21573108), Natural Science Foundation of Jiangsu Province (BK20180008 and BK20170644), and Fundamental Research Funds for the Central Universities.

Notes and references

1 Y. Yang, G. Y. Zheng and Y. Cui, *Chem. Soc. Rev.*, 2013, **42**, 3018–3032.
2 A. Manthiram, Y. Z. Fu, S. H. Chung, C. X. Zu and Y. S. Su, *Chem. Rev.*, 2014, **114**, 11751–11787.
3 Q. Pang, X. Liang, C. Y. Kwok and L. F. Nazar, *Nat. Energy*, 2016, **1**, 16132.
4 G. X. Li, Y. Gao, X. He, Q. Q. Huang, S. R. Chen, S.-H. Kim and D. H. Wang, *Nat. Commun.*, 2017, **8**, 850.
5 F. Wu, J. T. Lee, N. Nitta, H. Kim, O. Borodin and G. Yushin, *Adv. Mater.*, 2015, **27**, 101–108.
6 S. Y. Bai, X. Z. Liu, K. Zhu, S. C. Wu and H. S. Zhou, *Nat. Energy*, 2016, **1**, 16094.

7 Z. A. Ghazi, X. He, A. M. Khattak, N. A. Khan, B. Liang, A. Iqbal, J. Wang, H. Sin, L. Li and Z. Tang, *Adv. Mater.*, 2017, **29**, 1606817.
8 J. Sun, Y. Sun, M. Pasta, G. Zhou, Y. Li, W. Liu, F. Xiong and Y. Cui, *Adv. Mater.*, 2016, **28**, 9797–9803.
9 F. Pei, L. Lin, A. Fu, S. Mo, D. Ou, X. Fang and N. Zheng, *Joule*, 2018, **2**, 1–14.
10 W. Chen, T. Lei, T. Qian, W. Lv, W. He, C. Wu, X. Liu, J. Liu, B. Chen, C. Yan and J. Xiong, *Adv. Energy Mater.*, 2018, 1702889.
11 C. Milroy and A. Manthiram, *ACS Energy Lett.*, 2017, **2**, 2591–2597.
12 Z. Lin, Z. Liu, W. Fu, N. J. Dudney and C. Liang, *Adv. Funct. Mater.*, 2013, **23**, 1064–1069.
13 X. L. Ji, K. T. Lee and L. F. Nazar, *Nat. Mater.*, 2009, **8**, 500–506.
14 N. Jayaprakash, J. Shen, S. S. Moganty, A. Corona and L. A. Archer, *Angew. Chem., Int. Ed.*, 2011, **50**, 5904–5908.
15 F. Pei, L. Lin, D. Ou, Z. Zheng, S. Mo, X. Fang and N. Zheng, *Nat. Commun.*, 2017, **8**, 482.
16 G. Zhou, S. Pei, L. Li, D.-W. Wang, S. Wang, K. Huang, L.-C. Yin, F. Li and H.-M. Cheng, *Adv. Mater.*, 2014, **26**, 625–631.
17 X. Liang, C. Hart, Q. Pang, A. Garsuch, T. Weiss and L. F. Nazar, *Nat. Commun.*, 2015, **6**, 5682.
18 Z. Li, B. Y. Guan, J. T. Zhang and X. W. Lou, *Joule*, 2017, **1**, 1–12.
19 J. R. He, Y. F. Chen and A. Manthiram, *Energy Environ. Sci.*, 2018, **11**, 2560–2568.
20 J. R. He, Y. F. Chen, W. Q. Lv, K. C. Wen, C. Xu, W. L. Zhang, Y. R. Li, W. Qin and W. D. He, *ACS Nano*, 2016, **10**, 10981–10987.
21 J. R. He, L. Luo, Y. F. Chen and A. Manthiram, *Adv. Mater.*, 2017, **29**, 1702707.
22 J. R. He, G. Hartmann, M. Lee, G. S. Hwang, Y. F. Chen and A. Manthiram, *Energy Environ. Sci.*, 2019, **12**, 344–350.
23 J. R. He, Y. F. Chen and A. Manthiram, *Adv. Energy Mater.*, 2019, **9**, 1900584.
24 Y. X. Yin, S. Xin, Y. G. Guo and L. J. Wan, *Angew. Chem., Int. Ed.*, 2013, **52**, 13186–13200.
25 H.-J. Peng, J.-Q. Huang, X.-B. Cheng and Q. Zhang, *Adv. Energy Mater.*, 2017, **7**, 1700260.
26 C.-P. Yang, S. Xin, Y.-X. Yin, H. Ye, J. Zhang and Y.-G. Guo, *Angew. Chem., Int. Ed.*, 2013, **52**, 8363–8367.
27 A. Abouimrane, D. Dambournet, K. W. Chapman, P. J. Chupas, W. Weng and K. Amine, *J. Am. Chem. Soc.*, 2012, **134**, 4505–4508.
28 C. P. Yang, Y. X. Yin and Y. G. Guo, *J. Phys. Chem. Lett.*, 2015, **6**, 256–266.
29 J. R. He, Y. F. Chen, P. J. Li, F. Fu, Z. G. Wang and W. L. Zhang, *J. Mater. Chem. A*, 2015, **3**, 18605–18610.
30 J. R. He, W. Q. Lv, Y. F. Chen, J. Xiong, K. C. Wen, C. Xu, W. L. Zhang, Y. R. Li, W. Qin and W. D. He, *J. Mater. Chem. A*, 2018, **6**, 10466–10473.
31 Y. Cui, A. Abouimrane, J. Lu, T. Bolin, Y. Ren, W. Weng, C. Sun, V. A. Maroni, S. M. Heald and K. Amine, *J. Am. Chem. Soc.*, 2013, **135**, 8047–8056.
32 C. Liu, X. Huang, J. Wang, H. Song, Y. Yang, Y. Liu, J. Li, L. Wang and C. Yu, *Adv. Funct. Mater.*, 2017, **28**, 1705253.
33 Z. Li, J. T. Zhang, H. B. Wu and X. W. Lou, *Adv. Energy Mater.*, 2017, **7**, 1700281.
34 Z. Li, J. T. Zhang, B. Y. Guan, D. Wang, L. M. Liu and X. W. Lou, *Nat. Commun.*, 2016, **7**, 13065.
35 Q. Pang, D. Kundu, M. Cuisinier and L. F. Nazar, *Nat. Commun.*, 2014, **5**, 4759.
36 X. Liang, C. Hart, Q. Pang, A. Garsuch, T. Weiss and L. F. Nazar, *Nat. Commun.*, 2015, **6**, 5682.
37 S. Rehman, S. J. Guo and Y. L. Hou, *Adv. Mater.*, 2016, **28**, 3167.
38 S. Rehman, T. Y. Tang, Z. Ali, X. X. Huang and Y. L. Hou, *Small*, 2017, **13**, 1700087.
39 Z. W. Seh, J. H. Yu, W. Y. Li, P.-C. Hsu, H. Wang, Y. Sun, H. Yao, Q. Zhang and Y. Cui, *Nat. Commun.*, 2014, **5**, 5017.
40 Z. Yuan, H.-J. Peng, T.-Z. Hou, J.-Q. Huang, C.-M. Chen, D.-W. Wang, X.-B. Cheng, F. Wei and Q. Zhang, *Nano Lett.*, 2016, **16**, 519–527.
41 T. Chen, Z. W. Zhang, B. R. Cheng, R. P. Chen, Y. Hu, L. B. Ma, G. Y. Zhu, J. Liu and Z. Jin, *J. Am. Chem. Soc.*, 2017, **139**, 12710–12715.
42 T. Chen, L. B. Ma, B. R. Cheng, R. P. Chen, Y. Hu, G. Y. Zhu, Y. R. Wang, J. Liang, Z. X. Tie, J. Liu and Z. Jin, *Nano Energy*, 2017, **38**, 239–248.
43 Z. Cui, C. Zu, W. Zhou, A. Manthiram and J. B. Goodenough, *Adv. Mater.*, 2016, **28**, 6926.
44 Z. H. Sun, J. Q. Zhang, L. C. Yin, G. J. Hu, R. P. Fang, H.-M. Cheng and F. Li, *Nat. Commun.*, 2017, **8**, 14627.
45 D.-R. Deng, F. Xue, Y.-J. Jia, J.-C. Ye, C.-D. Bai, M.-S. Zheng and Q.-F. Dong, *ACS Nano*, 2017, **11**, 6031–6039.
46 P. Z. Chen, K. Xu, Y. Tong, X. L. Li, S. Tao, Z. W. Fang, W. S. Chu, X. Wu and C. Z. Wu, *Inorg. Chem. Front.*, 2016, **3**, 236–242.
47 H. Hu, B. Y. Guan and X. W. Lou, *Chem*, 2016, **1**, 102–113.
48 S. Xiang, H.-J. Qian, Y. Chen, K. Zhang, Y. Shi, W. Liu, H. Sun, H. Sun and B. Yang, *Chem. Mater.*, 2017, **29**, 6536–6543.
49 P. Z. Chen, K. Xu, Z. W. Fang, C. Z. Wu and Y. Xie, *Angew. Chem., Int. Ed.*, 2015, **54**, 14923–14927.
50 F. Maillard, A. Bonnefont, M. Chateneta, L. Guétazc, B. Doisneau-Cottigniesd, H. Roussele and U. Stimming, *Electrochim. Acta*, 2007, **53**, 811–822.
51 F. Zhou, Z. Li, X. Luo, T. Wu, B. Jiang, L.-L. Lu, H.-B. Yao, M. Antonietti and S.-H. Yu, *Nano Lett.*, 2018, **18**, 1035–1043.
52 I. Alstrup, I. Chorkendorff, R. Candia, B. Clausen and H. Topsoe, *J. Catal.*, 1982, **77**, 397–399.
53 Z. Li, J. T. Zhang, B. Y. Guan and X. W. Lou, *Angew. Chem., Int. Ed.*, 2017, **129**, 16219–16223.
54 Z. Zhang, S. Jiang, Y. Lai, J. Li, J. Song and J. Li, *J. Power Sources*, 2015, **284**, 95–102.
55 J. T. Zhang, Z. Li and X. W. Lou, *Angew. Chem., Int. Ed.*, 2017, **56**, 14107–14112.
56 Y. Wei, Y. Tao, Z. Kong, L. Liu, J. Wang, W. Qiao, L. Ling and D. Long, *Energy Storage Materials*, 2016, **5**, 171–179.
57 G. L. Xu, T. Y. Ma, C.-J. Sun, C. Luo, L. Cheng, Y. Ren, S. M. Heald, C. S. Wang, L. Curtiss, J. G. Wen, D. J. Miller, T. Li, X. B. Zuo, V. Petkov, Z. H. Chen and K. Amine, *Nano Lett.*, 2016, **16**, 2663–2673.